Mantle flow models with core-mantle boundary constraints and chemical heterogeneities in the lowermost mantle

B. Steinberger[1] and R. Holme[2]

[1] Decorrelation between s-wave and bulk sound velocities in the lowermost mantle and explicit density models based on seismic tomography give evidence for non-thermal lateral density variations in the lowermost mantle. Here we implement such variations in a numerical model of mantle flow driven by density anomalies which are derived from seismic tomography. In the lowermost ≈300 km, we either use both s-wave and bulk sound velocities to infer both thermal mantle density anomalies and non-thermal heterogeneities, or we assume that regions with s-wave speed anomalies below −1% have an additional non-thermal density anomaly. We predefine the shape of the viscosity profile in the upper mantle, transition zone and lower mantle, but absolute values of viscosity in the lithosphere, upper mantle, transition zone and lower mantle are free parameters. We use geoid, radial heat flux profile, viscosity "Haskell" average, core-mantle boundary (CMB) excess ellipticity, as well as (optionally) long-wavelength root mean square (RMS) CMB topography and reliable point estimates of CMB topography as constraints to optimize the model in parameter space in a least squares sense. We are able to obtain a reasonable fit to all data constraints. Computed RMS CMB topography is predominantly long-wavelength and with $1-1.5$ km RMS amplitude somewhat larger than the long-wavelength component inferred from seismology. Geoid variance reduction is 75 to 83% in our preferred parameter range. Best fit models have a viscosity maximum close to 10^{23} Pas about 600 km above the CMB, and a viscosity drop near the base of the mantle, corresponding to a thermal boundary layer about 300 km thick with temperature increase from ≈2500 to $3500-4000$ K.

1. Introduction

[2] Core-mantle boundary (CMB) topography is an important geophysical quantity for studies of core-mantle coupling [*Hide*, 1969; *Asari et al.*, 2006] and for the dynamics of flow at the top of the core and magnetic secular variation [*Kuang and Chao*, 2001]. Models of this topography can be obtained by seismology and by geodynamic modeling. Furthermore, CMB flattening can be determined by geodetic means. The purpose of this paper is to use available CMB topography (mainly ellipticity) and other (mainly geoid and heat flux) constraints in a geodynamic model that considers both thermal and chemical variation in the lower mantle and to provide a model of CMB topography consistent with these constraints.

[3] Evidence for non-thermal variations in the lowermost mantle comes from seismology: In the lowermost $300-400$ km of the mantle, S wave speed variations δv_S anti-correlate with bulk sound speed variations δv_C [*Su and Dziewonski*, 1997; *Masters et al.*, 2000]. Bulk sound speed is defined as $\sqrt{k_s/\rho}$ where k_s is adiabatic bulk modulus and ρ is density, hence δv_C can be derived from δv_S and P wave speed variations δv_P. If both δv_P and δv_S, and hence δv_C were linearly related to variations in temperature, they should be perfectly correlated. Furthermore, models of density determined using normal modes and S-wave tomography in the lowermost mantle are anti-correlated [*Ishii and Tromp*, 2004] whereas they should again be positively correlated, if they were both due to thermal variations.

[4] If there is a chemically distinct, heavier layer at the base of the mantle piled up below upwellings, normal stresses in the layer below, and hence the topography at the CMB are reduced. Non-thermal variations may, however, be both variations in chemistry and in phase. A post-perovskite phase boundary in the lowermost mantle has been recently predicted based on seismology [*Sidorin et al.*, 1999] and theoretically [*Oganov and Ono*, 2004] and confirmed experimentally [*Murakami et al.*, 2004]. If its Clapeyron slope is negative, like at the 660-km discontinuity, it will have also the effect of reducing the CMB topography. At present, its Clapeyron slope is not well known; however, calculations [*Tsuchiya et al.*, 2004],

---

[1]Center for Geodynamics, Geological Survey of Norway, Trondheim, Norway.
[2]Department of Earth and Ocean Sciences, University of Liverpool, UK.

experiments [*Hirose et al.*, 2006], seismological observations [*Sidorin et al.*, 1999] and geophysical constraints [*Hernlund and Labrosse*, 2007] indicate a large positive slope.

[5] Geodynamic models aim to predict flow in the mantle driven by density anomalies. Deformation of the bottom and top boundaries – CMB topography and dynamic surface topography – is predicted as part of the flow computation. Frequently, mantle density anomalies are derived from models of seismic tomography, and the assumption of viscous rheology, with only radial viscosity variations, is made. Lateral viscosity variations appear to have little effect on the resulting dynamic topography at the surface and the CMB [*Moucha et al.*, 2007]. Without considering lateral viscosity variations, flow caused by the density anomalies and the deformation of boundaries can be computed with a spectral method [*Hager and O'Connell*, 1979, 1981].

[6] Flow models may contain a number of free parameters, e.g., specifying the viscosity profile. Within the parameter space, a minimization of the misfit between certain model predictions and corresponding observations can then be carried out. This approach has led to a body of publications too large to be reviewed here. The work presented here mainly follows *Steinberger and Calderwood* [2006] which is briefly outlined in the following: S wave velocity anomalies from tomography models were converted to density anomalies, using "scaling factor" profiles derived from mineral physics, assuming both S wave velocity and density anomalies are due to thermal anomalies. The shape of the viscosity profile, i.e., relative viscosity variation with depth $\tilde{\eta}(z)$ in each layer (upper mantle, transition zone, lower mantle) was also defined motivated by mineral physics. However, absolute viscosity values for different layers were not prescribed. Rather they were treated as free model parameters. Three observational constraints (geoid, Haskell, heat flux; see section 2.3 for further explanation) were used. *Steinberger and Calderwood* [2006] found that a good fit to the geoid (up to about 80% variance reduction) along with a reasonable heat flux profile and appropriate viscosity "Haskell" average was possible, but for all models that yielded a good fit to geoid (in excess of about 75% variance reduction) and a reasonable heat flux profile, predicted CMB excess ellipticity was several times as high as observed. Even if excess ellipticity was additionally used as quantity to be fit in the optimization, results remained essentially unchanged: Models that fit geoid and heat flux well always give too large CMB flattening. A lower excess ellipticity can be obtained with a very low viscosity at the base of the mantle; however, this assumption leads to a substantial deterioration of fit to geoid and heat flux profile and within the parameter space investigated a model that gives an acceptable fit to geoid and CMB flattening could not be found. With other parameters the same as for their two preferred models, computed excess ellipticity varied between three and eight times the observed value for density models derived from different tomography models, mainly due to a large variation of the depth-dependent degree two order zero term among the tomography models used.

[7] This result possibly indicates that the density field is incorrect in a depth range where CMB topography is sensitive to density anomalies, and the geoid not very sensitive – especially in the lowermost mantle: The geoid contribution of density anomalies close to the CMB, and

of the deflection of the CMB itself largely cancel each other out, and therefore models based on the incorrect density field can still give a good fit to the geoid, but not to CMB ellipticity. An incorrect density field is obtained by converting seismic velocity to density using a thermal scaling factor, if there are non-thermal density variations. We choose here an approach that explicitly considers those. A different approach is to modify the velocity-to-density scaling profiles in the course of the iterations [e.g., *Forte and Mitrovica*, 2001; *Mitrovica and Forte*, 2004; *Simmons et al.*, 2006]. In this way, an extensive set of geophysical observables, including excess CMB ellipticity, can be fit without explicitly introducing non-thermal density variations. *Forte et al.* [1995] and *Simmons et al.* [2006] performed a joint inversion of seismic and geodynamic data, and could show that the tomography model can be modified to fit the excess ellipticity. The fit to the seismic data is not or only slightly degraded. *Simmons et al.* [2006] find the best fit to all data for whole mantle flow. In this case, their velocity-to-density scaling profile is close to zero in the lowermost mantle. A possible explanation for very low scaling factors is that positive thermal buoyancy is largely offset by negative chemical buoyancy. We hence see the two approaches of explicitly considering non-thermal density variations and modifying the scaling factor profile as complementary and not contradicting each other.

[8] Part of the mismatch in CMB topography (especially ellipticity) might also be caused by not considering lateral viscosity variations due to temperature variations: Although global flow structure appears to remain similar with and without lateral viscosity variations [e.g., *Becker*, 2006] and in isochemical convection, downwellings should always lead to negative (depressed) CMB topography, while upwellings cause positive (elevated) topography, cold, viscous downwellings should lead to a larger amount of CMB deflection than the hot, less-viscous upwellings, because the magnitude of stress (and hence topography) increases with viscosity [*Lassak et al.*, 2007]. Thus there is a possibility that the addition of lateral viscosity variations might change our interpretation.

2. Overview of Numerical Model

[9] The numerical model broadly follows *Steinberger and Calderwood* [2006]. New features introduced here are that we either use both δv_P and δv_S to derive density variations in the lowermost mantle, or only δv_S, but allow for additional non-thermal density variations in regions with velocity anomaly below -1%. We mainly use the models *smean* for δv_S and *pmean* for δv_P. They were derived by *Becker and Boschi* [2002] by respectively averaging over a number of published S and P wave models. Both our approaches lead to an additional free model parameter. As additional constraints in the optimization, we use CMB excess ellipticity, and optionally root mean square (RMS) CMB topography and CMB topography point data. The model, with particular emphasis on these new features, is explained in the following.

2.1. Relation Between Seismic Velocity, Thermal and Non-Thermal Density Anomalies

[10] In the bottom $\approx$300 km of the mantle δv_S and δv_C are strongly anticorrelated, and waveform modeling and
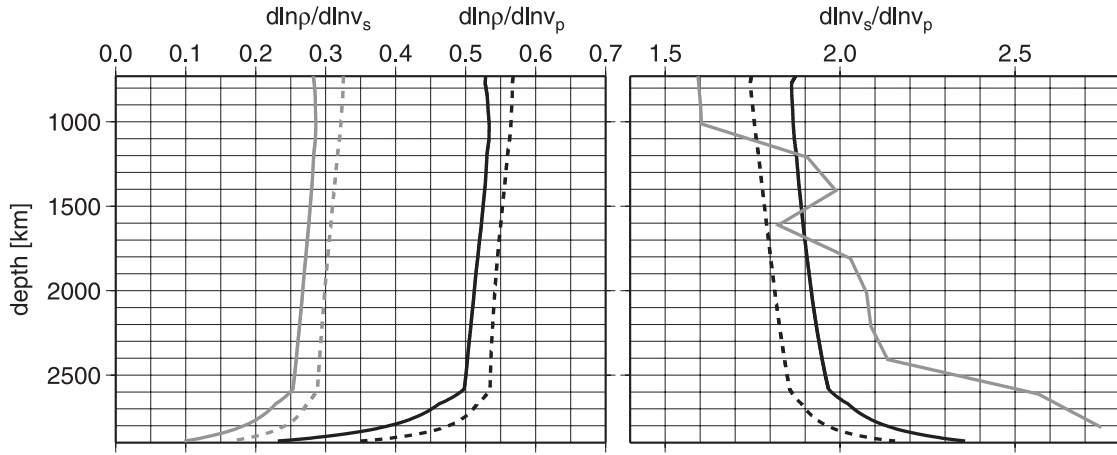
Figure 1. Left panel: Profiles of $(d \ln \rho / d \ln v_S)_{th}$, the scaling factor between density and S wave speed variations due to temperature variations (shaded lines) and $(d \ln \rho / d \ln v_P)_{th}$ for P waves (solid lines). A 300 km thick bottom thermal boundary layer and CMB temperature 3500 K are assumed; results remain very similar for 3700 K. Other assumptions are the same as in Model 2 (continuous lines) and the reference model (dashed lines) of *Steinberger and Calderwood* [2006] where the S wave profiles have been derived; P wave profiles are derived in this paper in analogy. Model 2 is mainly used in this paper. Right panel: $(d \ln v_S / d \ln v_P)_{th}$ for the same cases (solid lines). Also shown is the profile for the seismic model SB10L18 of *Master et al.* [2000] (shaded line).

traveltime analysis suggest very low velocity provinces with steeply dipping edges [*Wang and Wen*, 2004]. We therefore assume that in the bottom two layers of the tomography model *smean*, below 2584 km depth, δv_S and δv_P are due to variations both in temperature and non-thermal (chemical or phase) variations. For simplicity, in the layers above, where δv_S and δv_C are not strongly anticorrelated, we assume thermal anomalies only, based on S wave tomography. The depth range where our model allows for chemical variations is much smaller than in some other models [e.g., *Kellogg et al.*, 1999].

[11] We use two different approaches to determine total density anomalies. In the first approach (cases A and B), we write

$$\frac{\delta v_S}{v_S} = \frac{1}{(d \ln \rho / d \ln v_S)_{th}} \frac{\delta \rho}{\rho}\bigg|_{th} + \frac{1}{(d \ln \rho / d \ln v_S)_{nt}} \frac{\delta \rho}{\rho}\bigg|_{nt},$$
$$\frac{\delta v_P}{v_P} = \frac{1}{(d \ln \rho / d \ln v_P)_{th}} \frac{\delta \rho}{\rho}\bigg|_{th} + \frac{1}{(d \ln \rho / d \ln v_P)_{nt}} \frac{\delta \rho}{\rho}\bigg|_{nt}, \quad (1)$$

where *th* stands for thermal and *nt* for non-thermal. This approach of assuming a single contribution to variations in v_S, v_P and ρ besides variations in temperature, and relating these linearly, is simpler than other approaches recently proposed [*Forte and Mitrovica*, 2001; *Trampert et al.*, 2004].

[12] For $(d \ln \rho / d \ln v_S)_{th}$, the scaling factor between density and S wave velocity variations due to temperature variations, we use the radial profile derived by *Steinberger and Calderwood* [2006] (Figure 1). Here we derive the scaling factor for P wave velocity variations in the lower mantle in analogy: It is

$$(d \ln \rho / d \ln v_P)_{th} = -\alpha \bigg/ \left(\partial \ln \sqrt{\frac{k_s + 4\mu/3}{\rho}} \bigg/ \partial T \right)_p, \quad (2)$$

where the subscript p means partial derivative at constant pressure, μ is shear modulus and α is thermal expansivity. We also assume that the Q-factor for pure compressional motion is infinite. $(d \ln \rho / d \ln v_P)_{th}$ can thus be computed from k_s, μ, ρ, α, $\left(\frac{\partial \mu}{\partial T}\right)_P$ and $\left(\frac{\partial k_s}{\partial T}\right)_P$ as a function of depth z. k_s, μ and ρ are known relatively well, with values published, e.g., in PREM [*Dziewonski and Anderson*, 1981]. Models for α and $\left(\frac{\partial \mu}{\partial T}\right)_P$ were derived by *Steinberger and Calderwood* [2006] based on published literature, and

$$\left(\frac{\partial k_s}{\partial T}\right)_P \approx \frac{k_s(T(z) + \Delta T(z)) - k_s(T(z) - \Delta T(z))}{2\Delta T(z)} \quad (3)$$

can be derived in an entirely analogous manner: It is not directly determined at lower mantle pressure, but we can estimate the temperature derivative of adiabatic bulk modulus for lower mantle material extrapolated to zero pressure, $dk_{s0}/dT = 19$ MPa/K, based on parameters compiled by *Cammarano et al.* [2003] and the pyrolite phase diagram of *Ita and Stixrude* [1992].

[13] The two terms in the enumerator on the right hand side of equation (3) evaluated at zero pressure ($z = 0$) can then be written

$$k_s(T(0) \pm \Delta T(0)) = k_s(T(0)) \pm \Delta T(0) \cdot \frac{dk_{s0}}{dT} \quad (4)$$

and $k_s(T(z) \pm \Delta T(z))$ can be determined by integration along adiabats, if its radial derivatives are known. We follow *Duffy and Anderson* [1989] in estimating those radial derivatives based on the observation that in the PREM [*Dziewonski and Anderson*, 1981] lower mantle approximately

$$\frac{d \ln\left(\frac{dM}{dp}\right)}{d \ln \rho} \approx -1 \quad (5)$$

for both moduli $M = k_s$ and $M = \mu$. Making the implicit assumption that this also holds along isobars, they obtain

$$\frac{dM}{dz}(T(z) \pm \Delta T(z)) = \frac{dM}{dz}(T(z))(1 \pm \alpha(z) \Delta T(z)). \quad (6)$$

[14] The resulting profiles $(d \ln \rho / d \ln v_P)_{th}$ and $(d \ln v_S / d \ln v_P)_{th}$ are also shown in Figure 1. We obtain a ratio $(d \ln v_S / d \ln v_P)_{th} \approx 1.9$ throughout most of the lower mantle, but slightly higher in the bottom thermal boundary layer (2.1 and 2.0 at the depth of the *smean* bottom two layers 92 and 235 km above the CMB for "model 2" of *Steinberger and Calderwood* [2006], the model mainly to be used here). Results with parameters as in the reference model are very similar to *Brodholt et al.* [2007], while they are slightly higher for model 2, due to the somewhat larger assumed anelastic contribution. In both our models, $(d \ln v_S / d \ln v_P)_{th}$ is similar to the value obtained from tomography [*Masters et al.*, 2000] throughout most of the mantle, but substantially lower in the lowermost few hundred km. *Brodholt et al.* [2007] conclude that larger values observed by seismology must have another cause than temperature variations, most likely chemical variations; our conclusion will be the same.

[15] No prior assumptions about the two non-thermal scaling factors $(d \ln \rho / d \ln v_S)_{nt}$ and $(d \ln \rho / d \ln v_P)_{nt}$ are made. We can then derive from equation (1)

$$\frac{\delta\rho}{\rho} = \frac{\delta\rho}{\rho}\Big|_{nt} + \frac{\delta\rho}{\rho}\Big|_{th} = (1 - k_1) \cdot (d \ln \rho / d \ln v_S)_{th} \frac{\delta v_S}{v_S}$$
$$+ k_1 \cdot (d \ln \rho / d \ln v_P)_{th} \frac{\delta v_P}{v_P}.$$

k_1 can be expressed in terms of the four scaling factors (two thermal, two non-thermal), and is treated as a free parameter in the optimization. Only the total density anomalies in the lowermost mantle are determined as part of the optimization, not the thermal and non-thermal part separately.

[16] Since the degree two order zero term, which determines excess ellipticity, varies between tomography models, we modify this term in case B. We replace it in the bottom two layers of the *smean* model by the values corresponding to the model *S20RTS* of *Ritsema and van Heijst* [2000].

[17] We consider a further modeling case C, where we derive density variations based on only the s-wave model *smean*, but with the additional assumption that in the lowermost ≈ 300 km of the mantle regions with velocity anomaly below -1% are chemically distinct [*Burke et al.*, 2008; *Torsvik et al.*, 2006]. We therefore assume

$$\frac{\delta\rho}{\rho} = \frac{\delta\rho}{\rho}\Big|_{nt} + \frac{\delta\rho}{\rho}\Big|_{th} \quad \text{whereby} \quad \frac{\delta\rho}{\rho}\Big|_{th} = \left(\frac{d \ln \rho}{d \ln v_S}\right)_{th} \frac{\delta v_S}{v_S} \quad \text{and}$$
$$\frac{\delta\rho}{\rho}\Big|_{nt} = \begin{cases} k_1 & \text{if } \delta v_S / v_S < -1\% \\ 0 & \text{elsewhere} \end{cases}$$

and k_1 is again a free parameter.

[18] Utilizing tomography models in a more meaningful way beyond these simple conversions to density, e.g., considering their heterogeneous resolution, is beyond the scope of this paper.

2.2. Temperature and Viscosity Model

[19] Radial viscosity structure is expressed in the form

$$\eta(z) = q_i \cdot \eta_0 \cdot \tilde{\eta}(z). \quad (7)$$

$\tilde{\eta}(z)$ is the (dimensionless) relative viscosity variation with depth derived from the mineral physics model, η_0 is a constant (but model-dependent) scaling viscosity and q_i are four free parameters for the lithosphere ($i = 1$; 0–100 km depth), upper mantle ($i = 2$; 100–410 km), transition zone ($i = 3$; 410–660 km) and lower mantle ($i = 4$; below 660 km). Relative viscosity variations within a layer, i.e., due to the function $\tilde{\eta}(z)$ are particularly important in the lower mantle. There it is assumed that

$$\tilde{\eta}(z) = \exp\left(\frac{g \cdot T_m(z)}{T(z)}\right), \quad (8)$$

where T_m is melting temperature, T is (laterally averaged) actual temperature and g is a numerical constant. Profiles of T and T_m are shown in Figure 2. We use a melting temperature profile intermediate between experimentally determined profiles for lower mantle constituents $MgSiO_3$ perovskite [*Wang*, 1999] and MgO [*Zerr and Boehler*, 1994], which both look similar. This is considered appropriate by *Yamazaki and Karato* [2001].

[20] The actual temperature profile is assumed adiabatic except for thermal boundary layers; temperature in the bottom boundary layer is computed as a function of distance h from the boundary

$$T = T_{ad} + (T_{cmb} - T_{cmb,ad}) \cdot [1 - \text{erf}(h/d_{th})].$$

Here T_{ad} is the adiabatic temperature profile and $T_{cmb,ad}$ its value at the CMB (about 2500 K). d_{th} is thermal boundary layer thickness.

[21] T_{cmb} has been estimated to be 4000 ± 600 K [*Boehler*, 1996; *Schubert et al.*, 2001] and 3950 ± 200 K [*van der Hilst et al.*, 2007]. *Chudinovskikh and Boehler* [2007] determined eutectic melting temperatures in the system Fe-S and concluded that the temperature at the CMB could be substantially below 4000 K.

[22] It is expected that the ratio between T_m and T increases with depth through the lower mantle except for the thermal boundary layer at its base, where it decreases again. The temperature increase at the base of the mantle leads to a corresponding viscosity drop, according to equation (8). Thus we expect a viscosity "hump" in the lower mantle. The steepness of this hump depends on g, for which estimates also exist, but with considerable uncertainty. Viscosity profiles $\eta_0 \cdot \tilde{\eta}(z)$ (without the factors $q_1 \dots q_4$, i.e., not optimized) are also shown in Figure 2.

[23] Equation (8) can also be used to estimate lateral variations in viscosity which are not considered here: For a temperature variation δT away from the mean T, they are approximately a factor $\exp(g T_m \delta T / T^2)$ higher or lower. 1% seismic velocity anomaly should correspond to about $\delta T = 200$ K in the lower part of the mantle. With $g = 12$, $T_m =$
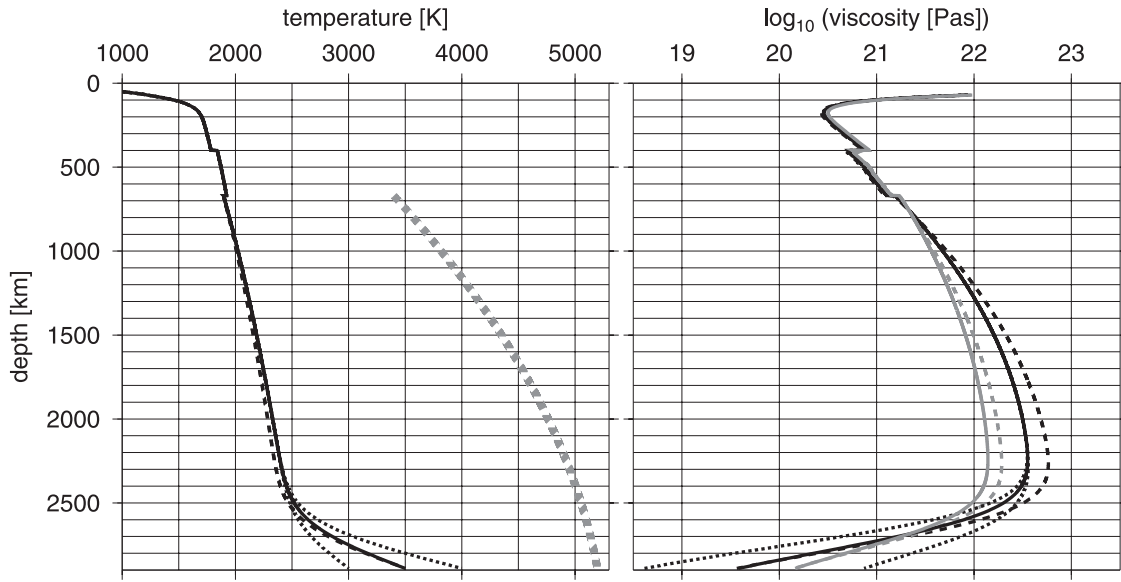
Figure 2. Left panel: Temperature profiles with 300 km thick bottom thermal boundary layer and CMB temperature 3500 K (continuous and dashed lines), and 3000 K and 4000 K (dotted lines). Other assumptions are the same as in Model 2 (continuous and dotted lines) and the reference model (dashed lines) of *Steinberger and Calderwood* [2006] where these profiles have been derived. Model 2 is mainly used here. Also shown is the melting temperature profile used (thick shaded dotted line). Right panel: Radial viscosity structures $\eta_0 \cdot \tilde{\eta}(z)$ for $g = 12$ (solid lines) and $g = 8$ (shaded lines); other modeling assumptions as in the left panel. This model is modified by factors q_1 to q_4 in the lithosphere, upper mantle, transition zone and lower mantle respectively to obtain best fit viscosity models.

5000 K and $T = 2500$ K as in Figure 2, this gives a factor ≈ 7 higher or lower viscosity. Lateral viscosity variations are thus probably quite substantial, perhaps of similar magnitude as the radial variations across the D'' layer, and should be considered in future studies.

2.3. Model Optimization

[24] The model is optimized by minimizing a misfit function

$$MF = P_1 + c_2 \cdot P_2 + \ldots + c_6 \cdot P_6, \qquad (9)$$

where $P_1, \ldots, P_6$ are "penalty functions" describing misfit to various observations, and $c_2, \ldots c_6$ are weighting factors. The first three were also used by *Steinberger and Calderwood* [2006] and are further discussed there. Here we introduce additional constraints related to CMB topography, especially ellipticity. For the most part and unless mentioned otherwise we use only the first four constraints, i.e., only consider CMB ellipticity as an additional constraint.

2.3.1. Misfit to Geoid

[25] The geoid has been often used as observational constraint, as it is sensitive to viscosity structure and flow, because both internal density anomalies and deformed boundaries contribute to geoid anomalies [*Richards and Hager*, 1984; *Ricard et al.*, 1984]. P_1 equals the variance of predicted minus observed geoid divided by the variance of the observed geoid, and thus describes the misfit to the geoid (degrees 1–15):

$$P_1 = \frac{\text{Var(Predicted} - \text{Observed)}}{\text{Var(Observed)}}.$$

$1 - P_1$ is referred to as geoid variance reduction. A free slip upper boundary is used for the geoid computation, because our approach only considers radial viscosity variations and a free upper boundary is consistent with this approach. *Thoraval and Richards* [1997] considered the effect of the upper boundary condition on the geoid, and found that a free slip yields the best fit. We expect that imposing platewise surface velocities without appropriate lithosphere rheology (i.e., weaker plate boundaries) may lead to artifacts in the geoid computation.

2.3.2. Misfit to Heat Flux Profile

[26] The fit to the geoid is only affected by relative viscosity variations; another constraint is needed for the absolute viscosity level: the radial heat flux profile should approximately fall between theoretical steady state profiles for internally and basally heated mantle, $\Phi_{ih}(r)$ and Φ_{bh}, with total mantle heat flux Φ_{bh} somewhere between 37 TW [*Schubert et al.*, 2001] based on a global heat flux around 44 TW [*Pollack et al.*, 1993; *Wei and Sandwell*, 2006] and 24 TW based on *Hofmeister* [2005]. These are present-day estimates, but the Earth's present-day heat flux is presumably similar to its long-term average [*Korenaga*, 2007]. We use here $\Phi_{bh} = 33$ TW, the mantle heat flux estimate of *Calderwood* [1999]. Φ_{bh} and the corresponding $\Phi_{ih}(r)$ are shown as thick dashed lines in Figure 3. $\Phi_{ih}(r)$ also takes heat conduction in the uppermost 200 km into account. We use the penalty function

$$P_2 = \int \frac{\max\left(\frac{\Phi(r) - \Phi_{bh}}{\Phi_{bh}}, 0\right)^2 + \max\left(\frac{\Phi_{ih}(r) - \Phi(r)}{\Phi_{bh}}, 0\right)^2}{2891 \text{ km}} dr. \qquad (10)$$
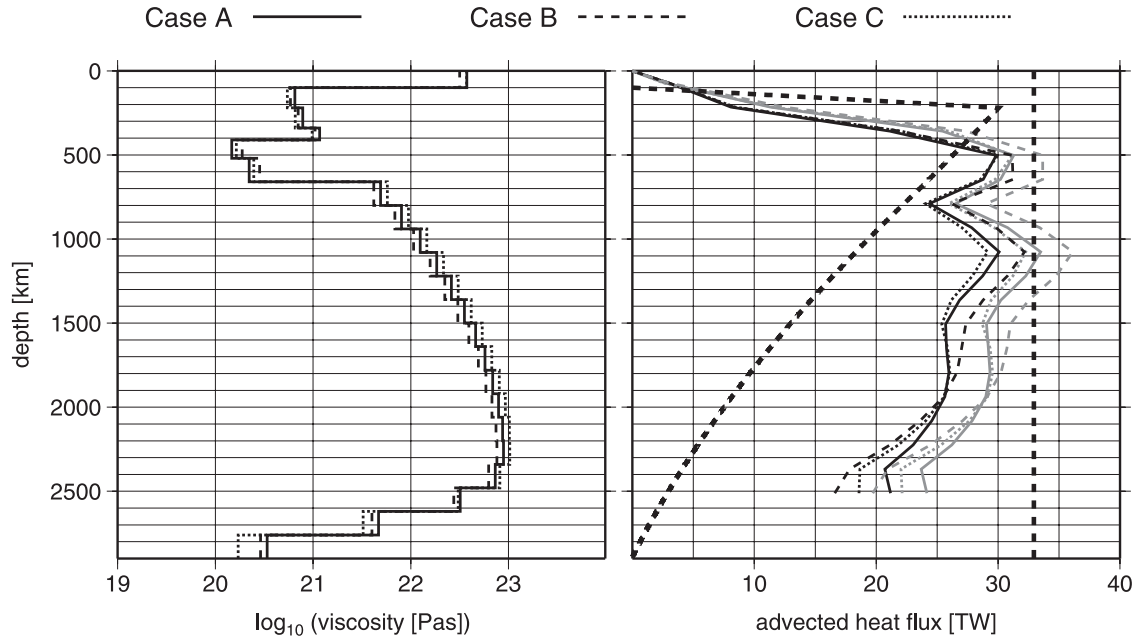
Figure 3. Best fit viscosity and radial heat flux profiles. Black continuous lines: Case A, thermal and non-thermal density variations in lowermost mantle inferred from p- and s-wave speed anomalies. Black dashed thin lines: Case B, as case A, but degree two order zero coefficients of the s-wave tomography model in the lowermost two layers are changed to values corresponding to model *S20RTS*. Black dotted lines: Case C, non-thermal density variations assumed for s-wave speed anomalies below −1%. For grey lines, heat flux is computed with free upper surface instead of prescribed plate motions. $l_{max} = 31$, $d_{th} = 300$ km and $g = 12$ in all cases; $T_{cmb} = 3500$ K in cases A and B, 3700 K in case C. Thick dashed lines are approximate theoretical steady state profiles for internally heated and basally heated mantle.

The advective heat flux profile $\Phi(r)$ is computed from the flow and density variations converted back to temperature variations. We mostly use present-day plate motions [*DeMets et al.*, 1990] as upper boundary condition for the heat flux computation, but also consider a free upper boundary.

2.3.3. Misfit to Haskell Condition

[27] The Haskell condition states that the logarithmic average of viscosity, weighted with an appropriate sensitivity kernel equals about 10^{21} Pas. We choose η_0 in equation (7) such that $\eta_0 \cdot \tilde{\eta}(z)$ satisfies the Haskell condition in the form defined by *Steinberger and Calderwood* [2006] with the sensitivity kernel for the Angerman River site given by *Mitrovica* [1996]. We define

$$P_3 = (1.67 \cdot q_2 + 1.33 \cdot q_3 + q_4)^2, \qquad (11)$$

because $\eta(z)$ in equation (7) also approximately fulfils the Haskell condition if the term in brackets in equation (11) is zero.

2.3.4. Misfit to CMB Ellipticity

[28] *Mathews et al.* [2002] obtain between 3.7% and 3.9% flattening in excess to equilibrium from modeling of the Earth's nutation and precession, corresponding to 328 to 346 m peak-to-valley amplitude of core radius variations, lower than the previous estimate 490 ± 110 m by *Gwinn et al.* [1986].

[29] Misfit to CMB ellipticity is considered by choosing

$$P_4 = (\epsilon/\epsilon_0 - 1)^2,$$

where ϵ is the computed CMB ellipticity and ϵ_0 is the observed excess ellipticity for which we use the value of *Mathews et al.* [2002].

2.3.5. Misfit to CMB Topography

[30] Optionally, we use RMS CMB topography as constraint. Seismic models suffer from significant non-uniqueness, with considerable covariance between topography and D″ structure. *Rodgers and Wahr* [1993] first noted a discrepancy between maps of CMB topography derived from *PcP* versus *PKP* data. It appears not possible to map CMB topography from *P*, *PcP*, and *PKP* data alone [*Soldati and Boschi*, 2005]. Underside reflected *PKKP* phases help to discriminate between CMB topography and D″ structure and have in addition a great sensitivity to CMB topography [*Garcia and Souriau*, 2000], but unfortunately do not sample globally, with reflection points concentrated in a few regions on the CMB. *Garcia and Souriau* [2000] suggest that, while it is not possible to determine CMB topography globally, it is possible to estimate RMS CMB topography. They find a CMB RMS topography of about 0.75 km, with about 0.5 km uncertainty, for wavelengths larger than 1200 km. The CMB topography $h_{cmb,rms}$ inferred

from our flow models has predominantly wavelength longer than that. Therefore we use the misfit function

$$P_5 = \left(\frac{h_{cmb,rms} - 0.75 \text{ km}}{0.5 \text{ km}} \right)^2.$$

[31] Optionally, we also use CMB topography point data [*Garcia and Souriau*, 1998]. These point data are restricted to patches of the CMB with sufficient density of underside reflection points of *PKKP* phases, which cover less than 5% of the CMB. Here we need to consider that the geodynamic model only treats long wavelength, whereas the point data also include shorter wavelengths. *Garcia and Souriau* [2000] find an RMS amplitude of about 2 km including short wavelength and about 0.75 km at long wavelength only. Hence there should be an RMS amplitude of about $\varepsilon_c = \sqrt{2 \cdot 2 - 0.75 \cdot 0.75}$ km $\approx$ 1.85 km at only wavelengths shorter than considered in our model, and we combine this value with the estimated errors of observed topography ε_o given by *Garcia and Souriau* [1998] to give an error estimate for the difference between observed and calculated topography: $\varepsilon_d = \sqrt{\varepsilon_c^2 + \varepsilon_o^2}$. We set P_6 equal to the normalized RMS difference (i.e., difference divided by ε_d) between calculated topography $h_{cmb,c}$ and observed topography $h_{cmb,o}$ minus its mean value $\overline{h_{cmb,o}}$

$$P_6 = \sqrt{\int \int \left(h_{cmb,o} - \overline{h_{cmb,o}} - h_{cmb,c} \right)^2 / \varepsilon_d^2 \, dA / A},$$

with integration over the patches where topography is given, with total area A. For CMB constraints the upper boundary condition has little effect and we also use a free upper boundary.

2.3.6. Weighting of Constraints

[32] We use weighting factors $c_2 = 4$, $c_3 = 1$, $c_4 = 1$; $c_5 = c_6 = 0$ (i.e., constraints 5 and 6 are not used in the optimization unless mentioned otherwise) or 1 (where specifically mentioned, see section 3.4). $c_2 = 4$ was found appropriate because it gives acceptable heat flux profiles that do not substantially exceed 33 TW at any depth, while at the same time the fit to the geoid does not decrease by more than a few per cent compared to the case without heat flux profile constraint; results stay very similar even if this constraint is weighted two or three times more strongly. $c_3 = 1$ was found appropriate because the Haskell constraint is always fit very well regardless of the value of c_3 [*Steinberger and Calderwood*, 2006]. If constraints 5 and 6 are not used, then excess ellipticity can be fit very well with $c_4 = 1$; results remain almost unchanged if this constraint is weighted two or three times more heavily or only half as strongly.

3. Results

3.1. Representative Cases

[33] Resulting best fit viscosity structures and radial heat flux profiles for representative (not best fit) cases are shown in Figure 3: $T_{cmb} = 3500-3700$ K approximately agrees, within uncertainties, with other estimates of CMB temper-

atures, $d_{th} = 300$ km is similar to the thickness of the layer at the base of the mantle where lateral variations in chemistry are assumed and $g = 12$ follows *Yamazaki and Karato* [2001]. We obtain geoid variance reductions 76.5%, 71.5% and 82.3% for cases A, B and C. Case B is further discussed in section 3.5. The viscosity drop in the transition zone is not a robust feature of our model: results with lowest viscosity below the lithosphere tend to give almost as high variance reduction. The profile of advected heat flux is only plotted in the depth range where thermal anomalies only are assumed: Since in case A and B we only compute total density anomalies, and do not distinguish between thermal and compositional ones at the base of the mantle, computation of the heat flux profile is not possible there. The predicted heat flux profiles are intermediate between the steady state profiles for internally heated and basally heated mantle, except in the uppermost $\approx$500 km where they are too low. Reasons for this discrepancy are discussed by *Steinberger and Calderwood* [2006]. In particular, temperature anomalies and flow varying on a length scale shorter than resolvable by seismic tomography could contribute to the heat flow. Although we regard prescribed plate motions as the most appropriate boundary condition for computing heat flux, it is not consistent with the boundary condition chosen for the geoid computation. Therefore we also compute heat flux profiles with free upper surface. The profiles (grey lines in Figure 3) remain very similar and we hence do not expect that the choice of upper boundary condition for the heat flux computation affects any of our results in a major way, or affects any of our conclusions. Both the Haskell constraint and CMB ellipticity can be almost perfectly fit, i.e., both P_3 and P_4 are close to zero.

[34] The implied density fields in the bottom two layers, where chemical variations are assumed, are shown in Figure 4. The most important features are the two large positive anomalies beneath the Pacific and Africa, roughly underlying the two large-scale upwellings of the computed flow field in the overlying mantle, in those regions where the horizontal flow field converges. Qualitatively, these large-scale positive density anomalies can be interpreted as a chemically distinct layer at the base of the mantle that is driven by large-scale flow toward the base of large-scale upwellings and hence has accumulated and become thicker there: While the model assumes non-thermal anomalies throughout the bottom $\approx$300 km of the mantle, in the real Earth this might actually more closely correspond to an undulating, possibly diffuse, chemical boundary. The depth range where these variations occur is also uncertain to some degree. We therefore performed additional computations where we allow for chemical variations over a larger depth range. Results remain similar overall, but with slightly decreased fit to geoid, and overall fit, for larger depth range. Inferred non-thermal density variations become somewhat smaller if they are allowed over a larger depth range. The left panel in the second row of Figure 4 shows the density field in case A filtered to only spherical harmonic degrees 2, 4, and 6. Compared to the explicit density model of *Ishii and Tromp* [2004] (second row right panel), derived from seismic tomography and free oscillations, at these degrees our computed density anomalies have only about half the amplitude. The correlation coefficient between the two density models is 0.33. The rather low correlation is in part
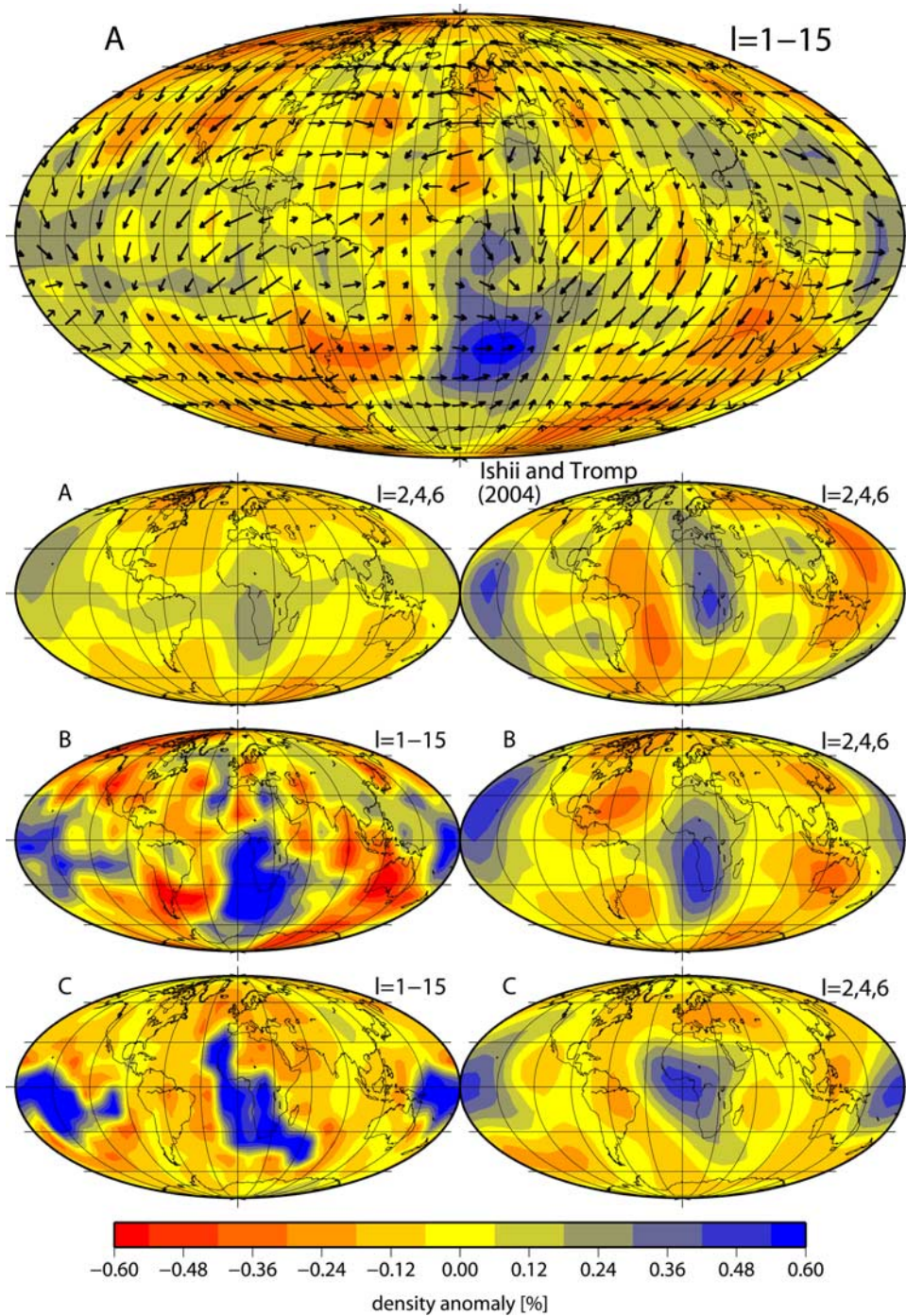
Figure 4. Top panel: Implied density anomaly for spherical harmonic degrees 1 to 15, averaged over the bottom two layers (307 km) of the model for case A (solid lines in Figure 3). Computed flow is shown 379 km above the CMB; 1 cm/a corresponds to 5 degrees of arc. Second row left panel: same density field filtered to spherical harmonic degrees 2, 4, and 6. Second row right panel: the model of *Ishii and Tromp* [2004], for the same spherical harmonic degrees and depth range. Third row and fourth row: Implied density anomaly for spherical harmonic degrees 1 to 15 (left), and degrees 2, 4, and 6 only (right) averaged over the bottom 307 km for cases B and C (dashed and dotted lines in Figure 3).

due to a band of high densities along the equator in our model which allows us to fit CMB ellipticity. A somewhat larger CMB ellipticity could presumably give a somewhat higher correlation. For comparison, implied density fields for cases B and C are shown in the two bottom rows. In these cases, density fields filtered to only spherical harmonic degrees 2, 4, and 6 have similar amplitude as the *Ishii and Tromp* [2004] model; correlation coefficients with the latter are 0.40 and 0.34.
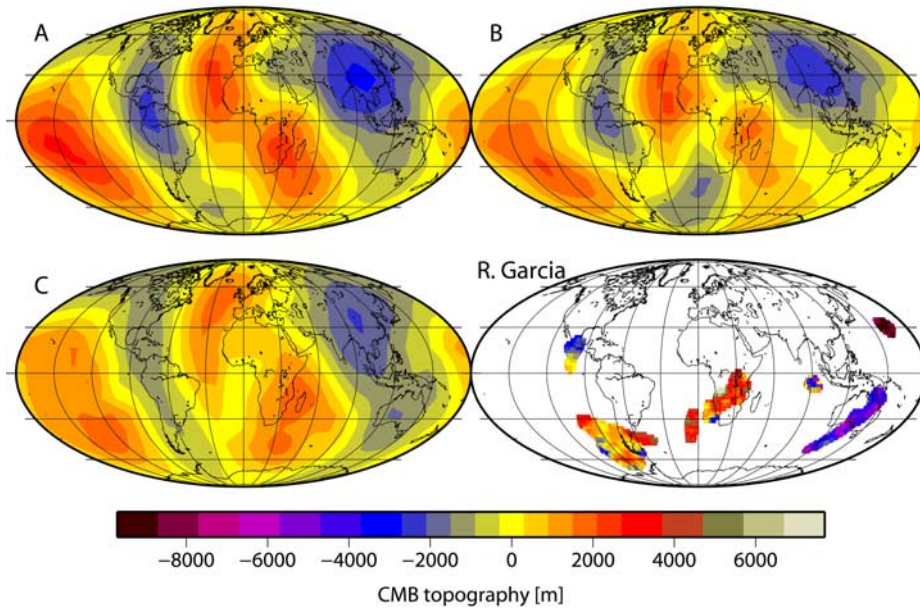
Figure 5. Top left, top right and bottom left: Predicted CMB topography for the same cases A, B, and C ($l = 1-15$) as in Figure 4. Bottom right: CMB topography obtained by *Garcia and Souriau* [1998] in regions where *PKKP* CMB underside reflection points are concentrated.

[35] Predicted CMB topography for the same cases is shown in Figure 5. The pattern of predicted CMB topography is rather similar in all three cases. It is dominated by very long wavelengths, because the tomography models on which the prediction is based are also dominated by very long wavelengths in the lowermost mantle. Predicted RMS amplitudes are 1.33 km in case A, 1.05 km in case B and 1.03 km in case C− somewhat larger than the long-wavelength result of *Garcia and Souriau* [2000]. For comparison, CMB topography point data from *Garcia and Souriau* [1998] in those regions with sufficient density of *PKKP* reflection points are shown in the bottom right panel. Visual agreement is not particularly good, but at least, more often than not, predicted topography is positive where observations show positive topography, and negative where observations show negative topography. It is again evident that the observed topography has much more short-wavelength structure, and, as mentioned, this is probably responsible for much of the discrepancy. This fact has already been considered in our topography error estimate. Hence we obtain a normalized RMS difference $P_6 = 1.0$ in cases A and C and 1.1 in case B, i.e., differences are about as large as should be expected. Results were also visually compared to those of *Doornbos and Hilton* [1989] and *Sze and van der Hilst* [2003], who also included *PKKP* phases in their analysis. Neither of these models bears a striking resemblance to our prediction, but on the other hand, the three seismological CMB topography models don't look very similar to each other either.

3.2. Dependence on the Shape of Lower Mantle Viscosity Profile

[36] Neither the thickness nor the temperature drop of the thermal boundary layer at the base of the mantle are known a priori. In particular, if, as surmised here, some material at the base of the mantle is heavier because of different composition and hence tends to remain there, both the thickness and the temperature drop of the thermal boundary layer at the base of the mantle could be larger than in the case of pure thermal convection. Furthermore the value of g, hence the steepness of the viscosity hump in the lower mantle according to equation (8) is rather uncertain. It would be possible to treat thickness and temperature drop of the thermal boundary layer, as well as the value of g, as additional free parameters in the optimization. However, we find another approach more instructive: We compute best fit models with the five free parameters described above on 2-D cross sections through a 3-D grid covering a reasonable range of thermal boundary layer thickness d_{th} from 100 to 350 km, CMB temperatures T_{cmb} from 3000 to 4000 K and g from 4 to 20.

[37] While the misfit function equation (9) describes overall model fit, it is also quite undescriptive, and, given that weighting factors $c_1 \ldots c_6$ are somewhat arbitrary, it is not particularly meaningful which exact combination of parameters gives the best overall misfit. We therefore do not show contour plots of overall misfit. Rather we consider the individual misfit contributions, and show contour plots for geoid variance reduction and CMB RMS topography, which we consider illustrative.

3.2.1. Fit to Geoid

[38] Resulting variance reduction on three 2-D cross sections through $d_{th} - T_{cmb} - g$−space with other assumptions as in case A is shown in Figure 6. For the top left panel we use $g = 12$ following *Yamazaki and Karato* [2001]. Comparison with our previous results purely based on S wave tomography, assuming purely thermal anomalies [*Steinberger and Calderwood*, 2006, Figure 14] shows that we can achieve essentially the same variance reduction of up to about 77%. However, in addition we can obtain a good fit to CMB excess ellipticity. This was not possible in the work of *Steinberger and Calderwood* [2006], where the
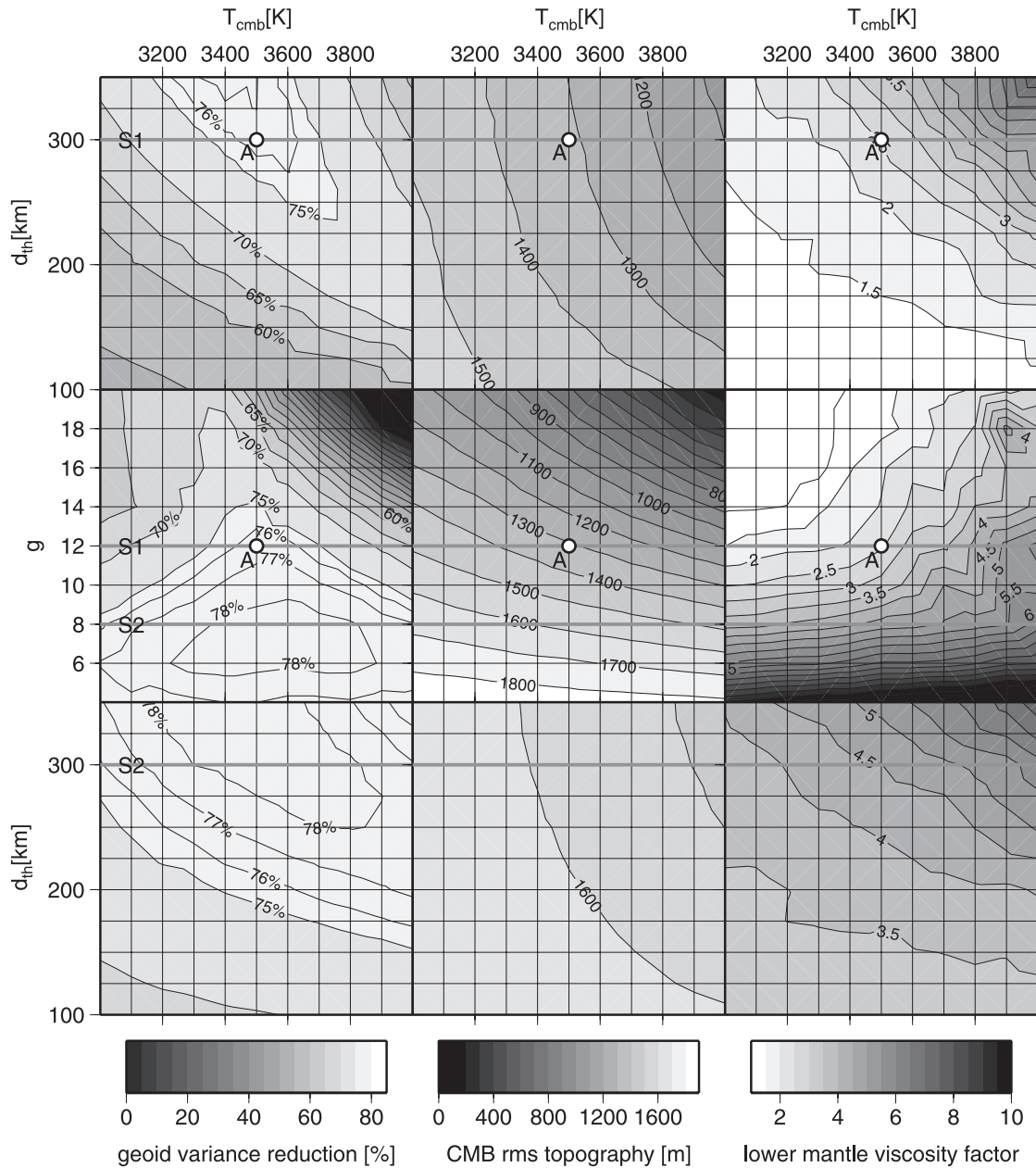
Figure 6. Left panels: Geoid variance reduction as a function of d_{th} and T_{cmb} with $g = 12$ (top), as a function of T_{cmb} and g with $d_{th} = 300$ km (middle), and as a function of d_{th} and T_{cmb} with $g = 8$ (bottom). Middle panels: predicted CMB RMS topography for the same cross sections. Right panels: Lower mantle viscosity factor q_4 for the same cross sections. These are cross sections through a 3-D parameter space intersecting along the lines S1 and S2. For each point, the model has been optimized by minimizing the misfit function in (another) 5-D parameter space. Other modeling assumptions are the same as in the case A model shown in Figures 3–5, which is indicated by circles.

implied CMB excess ellipticity was always much too large. We find that the optimized models fit excess ellipticity well for the entire array, and it appears that requiring a good fit to excess ellipticity does not significantly increase the misfit to geoid and heat flux profile. There is a tradeoff for the best fit to the geoid between d_{th} and T_{cmb}: Higher T_{cmb} around 4000 K gives the best fit with smaller d_{th} around 200 km, and lower T_{cmb} around 3400 K gives the best fit with larger d_{th} around 350 km. With $d_{th} = 300$ km and $g = 12$ as in Figure 3, $T_{cmb} = 3500$ K does indeed give higher variance

reduction than higher or lower T_{cmb} – about 76.5%, compared to less than 70% for both $T_{cmb} = 3000$ K and 4000 K, corresponding to smaller or larger viscosity decrease in D″. Compared with the models assuming thermal anomalies only, the area of best fit models has been shifted toward larger d_{th} and larger T_{cmb}.

[39] In the middle left panel of Figure 6 we show a cross section with $d_{th} = 300$ km which allows rather high variance reduction in the top left panel, i.e., this cross section and the previous one intersect along the line for $d_{th} = 300$ km

and $g = 12$. A good fit to the geoid can be achieved for a rather wide range of parameters that are consistent with observational constraints, hence a rather wide range of viscosity profile shapes. However, in the corner of the array with large g and high T_{cmb}, which corresponds to the strongest viscosity drop in the lowermost mantle, variance reduction is very low. The highest variance reduction in this panel is obtained for a shallow viscosity hump in the lower mantle corresponding to g around 6 to 8.

[40] Therefore the bottom left panel shows another cross section with $g = 8$, i.e., intersecting with the previous one along the line for $d_{th} = 300$ km and $g = 8$ and parallel to the first one. Results stay similar to the first one, but the area with high variance reduction above about 75% is much larger.

[41] For all three panels, in the areas with variance reduction above 75%, the best fit models have the lowest viscosity in the transition zone. If the optimization is essentially restricted to models with the lowest viscosity in the asthenosphere (by penalizing, in the misfit function, a viscosity drop in the transition zone), variance reduction is somewhat reduced (about 72% maximum). Variance reduction is also slightly lower (by a few per cent), if modeling assumptions other than the values of T_{cmb}, d_{th} and g, which are variable in the arrays shown, are replaced by those of the reference model of *Steinberger and Calderwood* [2006].

3.2.2. Heat Flux Profiles, Haskell Viscosity Average, and CMB Ellipticity

[42] The heat flux profiles in Figure 3 were found to be fairly representative for results with a high geoid variance reduction (above ≈75%). Contour plots of heat flow misfit function P_2 were plotted by *Steinberger and Calderwood* [2006] indicating that heat flow misfit remains similar for models with high geoid variance reduction, and mainly depends on whether the lowest viscosity occurs in the asthenosphere (giving lower heat flow misfit, but also lower variance reduction) or the transition zone. Results obtained here remain essentially the same in that respect, and for these reasons we do not show heat flow misfit contours.

[43] The Haskell constraint can be always very closely matched, and the observed excess ellipticity could also be approximately matched for all cases where a high variance reduction was achieved. Therefore results do not depend much on how strongly the corresponding constraints are weighted, weighting factors $c_3 = 1$ and $c_4 = 1$ are appropriate and contour plots of corresponding misfit functions P_3 and P_4 are not shown.

3.2.3. CMB Topography

[44] The middle column of Figure 6 shows, for the same cross sections, computed CMB RMS amplitude (which here was not used as a constraint, i.e., $c_5 = 0$ in equation (9)). In areas with high variance reduction above 75% CMB RMS amplitude varies between about 1200 and 1800 m, somewhat more than the approximately 750 m obtained by *Garcia and Souriau* [2000] based on observations. The disagreement with this number becomes smaller for larger g, larger d_{th} and larger T_{cmb}; however, an RMS amplitude of less than about 1000 m, which would approximately agree with the observation-based value, within its uncertainties, is only obtained with substantially reduced variance reduction. There is a tradeoff between higher variance reduction and lower CMB RMS amplitude, less discrepant with observa-

tions. As in the representative case A discussed above, normalized RMS misfit to CMB topography point data is about 1.0, with little variation over the arrays considered (and is therefore not shown as contour plots either).

3.3. Absolute Viscosity Values

[45] The values of q_4 shown in the right column of Figure 6 allow, in combination with Figure 2 and equation (7), determination of viscosity in the lower mantle. Typically, in areas with high variance reduction, the viscosity maximum in the lower mantle is about 10^{23} Pas, but there is a tradeoff between maximum viscosity and the viscosity drop in the lowermost mantle: The higher and wider this viscosity drop is (corresponding to larger values of T_{cmb} and d_{th}) the higher is also the viscosity maximum. Furthermore, the steeper the viscosity hump, the smaller is the viscosity just below the 660-km discontinuity.

[46] As mentioned, our models do not strongly constrain q_2 and q_3, i.e., the viscosity profile in the upper mantle: similar results are obtained for viscosity minimum below the lithosphere or in the transition zone. Thus corresponding plots of q_2 and q_3 are not very instructive and thus not included. Likewise, q_1 is not plotted, as the treatment of the lithosphere as viscous layer is a simplification, but probably acceptable in the context of this paper as the computed CMB topography remains very similar regardless of the top boundary condition (prescribed plate motions or free surface).

3.4. Tradeoff Between Excess Ellipticity, and CMB Topography

[47] The results described so far were obtained with $c_5 = c_6 = 0$ in equation (9), i.e., misfit to RMS CMB topography and CMB topography point data was not included in the optimization. We find that including RMS topography in the optimization ($c_5 = 1$) reduces RMS topography of optimized models by about 100 m, but this comes at the expense of also reducing excess ellipticity to about 80% of its observed value, whereas otherwise we could obtain a perfect fit. This happens because, within our model parameter space, we can easily vary the amplitude of CMB topography, but the pattern tends to stay very similar. There is a tradeoff between fit to excess ellipticity and CMB RMS topography, with better fit to the latter for larger c_5. If we also include CMB topography point data in the optimization ($c_6 = 1$) we find that results change only slightly, and there is no significant improvement of fit to point data.

3.5. Dependence on Tomography Model

[48] An additional uncertainty in our model comes from the variation between the different tomography models. Corresponding computations with P and S wave velocities of model *SB10L18* [*Masters et al.*, 2000], which was obtained in a joint inversion for both types of waves, and a mixture of the two models, *SB10L18* in the bottom two layers (evaluated 81 and 279 km above the CMB, corresponding to the bottom 329 km of the mantle) and *smean* above, yielded less satisfactory results.

[49] In the context of this paper, the spherical harmonic degree two order zero term is of particular interest, since it determines CMB excess ellipticity. To explore the effect of this uncertainty, we have run another suite of models where,
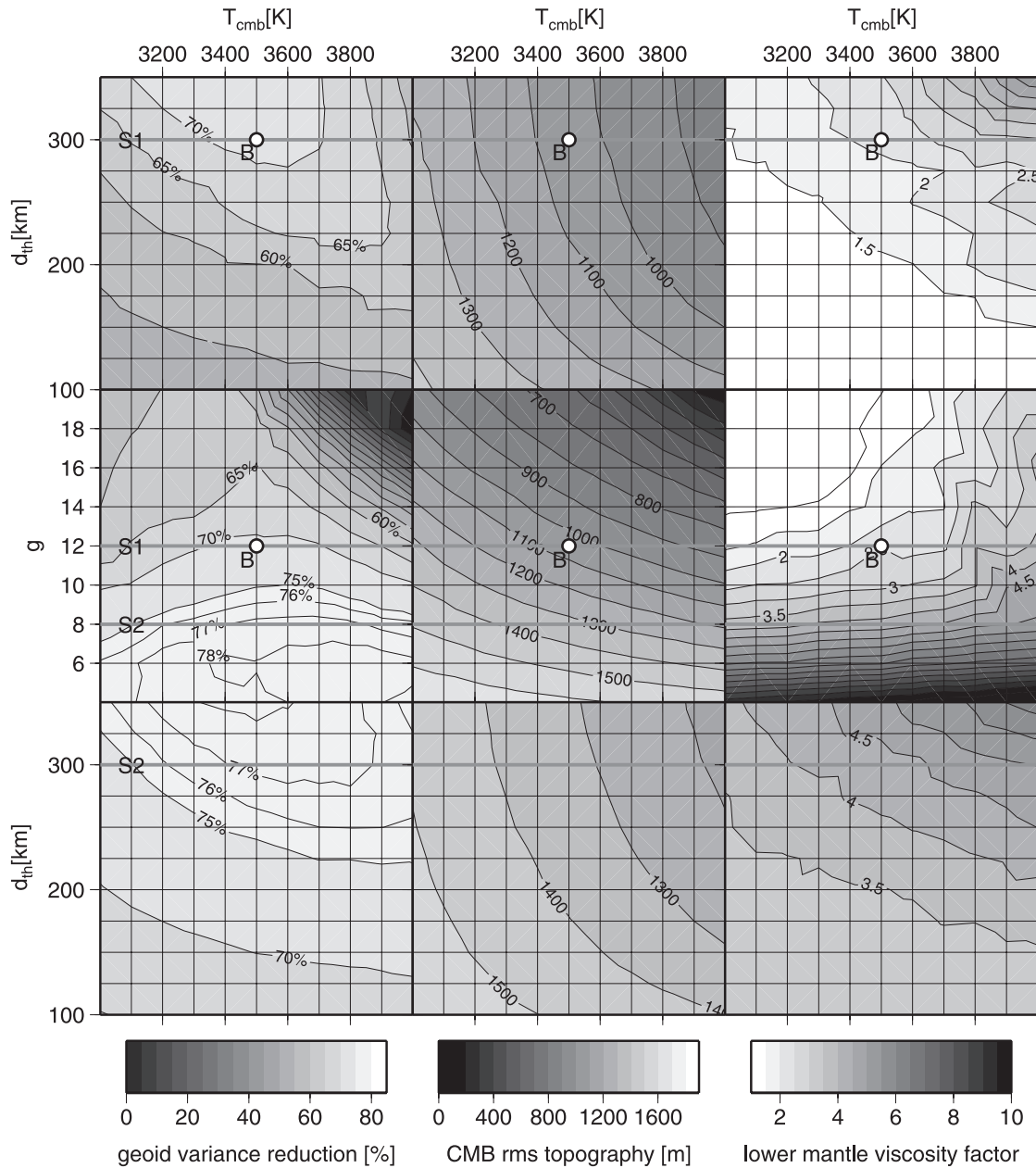
Figure 7. Same as Figure 6 but with degree two order zero coefficients of the tomography model in the lowermost two layers changed to the values corresponding to model *S20RTS* [*Ritsema and van Heijst*, 2000] (as in the case B model, which is indicated by circles).

as in case B, we have replaced the degree two order zero term in the bottom two layers of the *smean* model by values corresponding to the model *S20RTS* by *Ritsema and van Heijst* [2000]. That is, we have reduced its value by about 44% in the layer 92 km above the CMB, and by about 38% in the layer 235 km above. Results in Figure 7 show that, with this change, we now obtain somewhat lower CMB topography RMS amplitudes, while almost exactly fitting CMB excess ellipticity, but at the expense of somewhat lower variance reduction, in particular for the top panels. Misfit to CMB topography point data is slightly increased to about 1.1 to 1.2 in this case.

[50] The third row panels of Figure 4 show that, in this case (and again with $g = 12$, $d_{th} = 300$ km, $T_{cmb} = 3500$ K)

the amplitude of the predicted density anomaly in the lowermost mantle is increased by almost a factor 2, but the pattern remains very similar. When filtered to degrees 2, 4, and 6 only, the amplitude is now very similar to *Ishii and Tromp* [2004]; the two density models have a correlation coefficient of 0.40. The corresponding predicted CMB topography is shown in the bottom left panel of Figure 5. Its RMS amplitude is reduced by ≈20% to 1.05 km, but the pattern again remains very similar. More generally, we find that the predicted pattern of density anomalies in the lowermost mantle and CMB topography are rather robust features of our model: They look rather similar for different combinations of reasonable values of g, d_{th}, T_{cmb} and (d ln
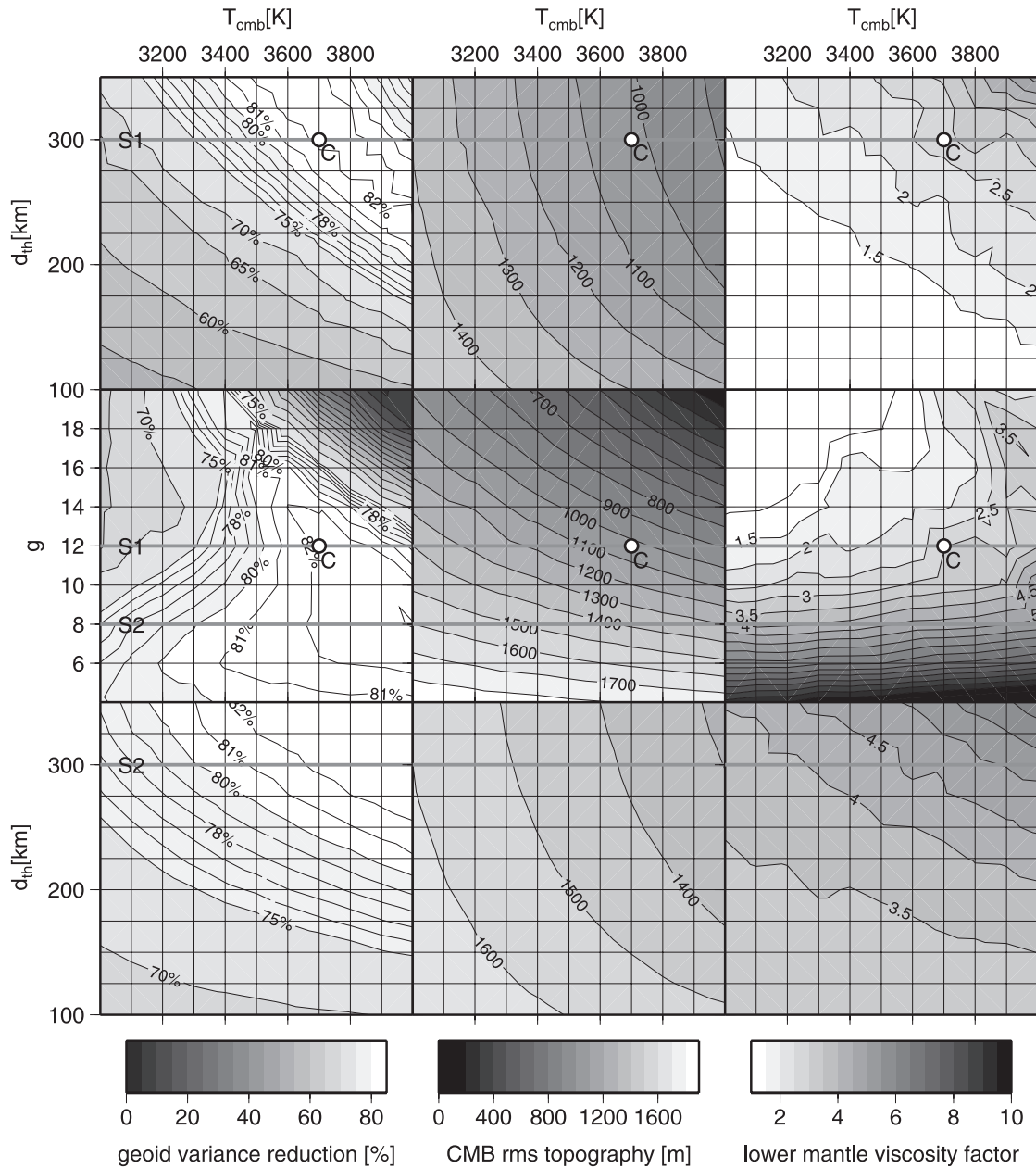
Figure 8. As in Figure 6, but with other modeling assumptions as in the case C model, which is indicated by circles.

$v_P/d \ln v_S)_{th}$ that yield low misfit and high variance reduction.

[51] Finally Figure 8 shows results that, as in case C, were derived based on the *smean* tomography model only, but allowing for additional non-thermal density variations in the lowermost two layers. For this case, we obtain the highest variance reductions – up to 83% – while CMB topography RMS amplitudes are less than in Figure 6 and similar to Figure 7. CMB excess ellipticity is again fit well, and misfit to CMB topography point data is about 1.0 to 1.1 in this case. Implied chemical density variation k_1 is about 1.2%. Parameter ranges for the the best fit models remain similar to the other two cases. We also performed computations where we allow for non-thermal variations in more than the bottom two layers. Results remain again similar,

but with somewhat lower chemical density variation and somewhat lower variance reduction obtained.

4. Discussion, Conclusions and Outlook

[52] We have presented here a model of mantle density, viscous flow and boundary deformation that is based on seismic tomography and mineral physics. As a specific feature, we assume that density variations in the lowermost ≈ 300 km of the mantle are due to both chemical and thermal anomalies, and we use, in our model cases A and B, both P and S wave tomography models to infer these density variations, whereas in model case C we only use an S wave model. With this approach, we can find results that, in addition to successfully reproducing essential features of

the long-wavelength geoid (about 77% variance reduction for degrees 1 to 15 in case A, 82% in case C), yielding a reasonable heat flux profile, and having an average viscosity that is in accord with postglacial rebound, also reproduce CMB excess ellipticity.

[53] We did not attempt to fit plate velocities, dynamic surface topography or seismic anisotropy. Plate velocities do not provide a strong constraint to flow models, because they are rather easily fit with a variety of assumptions [*Becker and O'Connell*, 2001]. Moreover, *Steiner and Conrad* [2007] find that a good fit to observed plate motions can be obtained from flow driven by positive density anomalies (corresponding to slabs) inferred from tomography, and that adding negative anomalies generally degrades the fit. Thus our approach, which uses the same scaling from seismic velocity to density anomalies for both positive and negative anomalies except in the lowermost mantle would presumably have to be modified in order to make plate velocities a meaningful constraint. Dynamic topography is rather insensitive to variations of viscosity with depth [*Steinberger et al.*, 2001] and is furthermore not well defined by observations. Seismic anisotropy promises to provide an important constraint on mantle flow [*Behn et al.*, 2004; *Becker et al.*, 2006].

[54] Models with only thermal variations but otherwise based on the same assumptions always yielded excess ellipticity several times as large as observed [*Steinberger and Calderwood*, 2006]. If, different from our approach, velocity-to-density scaling profiles are modified in the course of the iteration, it is possible to fit a number of constraints including CMB ellipticity without explicit non-thermal density variations [*Forte and Mitrovica*, 2001; *Mitrovica and Forte*, 2004; *Simmons et al.*, 2006]. In this case, low scaling factors obtained in the lowermost mantle may also be indicative of non-thermal density variations. It remains to be tested whether it would still be possible, even without modifying velocity-to-density scaling profiles, to modify tomography models such that excess ellipticity is matched without degrading the fit to seismic data, and without invoking non-thermal variations, with the method pioneered by *Forte et al.* [1995], and recently used by *Simmons et al.* [2006].

[55] Our resulting best fit viscosity profiles remain similar to the model with only thermal variations except that the low-viscosity layer at the base of the mantle is somewhat thicker in the models with chemical variations. In the lower part of the mantle, they are also very similar to the profiles inferred by *Mitrovica and Forte* [2004] based upon joint inversion of convection and glacial isostatic adjustment data, and by *Simmons et al.* [2006] with jointly fitting seismic and geodynamic data.

[56] In our models with non-thermal variations, the predicted pattern of CMB topography remains the same as for only thermal variations, and is also similar to the pattern computed by *Forte et al.* [1995] and *Moucha et al.* [2007]. The amplitude is about 6 km peak-to-valley, about a factor 2 less than by *Forte et al.* [1995] and in our own computations without non-thermal variations. Topography ≈ -8 km off the coast of Japan obtained by *Garcia and Souriau* [1998] closely matches the minimum of -6 km in the model of *Forte et al.* [1995]. The lower amplitude in our models with non-thermal variations is caused by the posi-

tive density anomalies inferred below large-scale upwellings, which cause normal stresses and topography at the CMB to be reduced in these regions. Because the respective kernels peak at the boundary, the effect of density anomalies close to the boundaries on topography is strong. On the other hand, geoid kernels go to zero at the boundary. Hence the different density structure inferred, compared with the case with thermal anomalies only, does not strongly affect the fit to the geoid.

[57] Results will presumably be affected by lateral variations in viscosity, which were not considered here: *Lassak et al.* [2007] found that cold, viscous downwellings lead to a larger amount of CMB deflection than the hot, less-viscous upwellings, because the magnitude of stress (and hence topography) increases with viscosity. However, in isochemical convection, downwellings always lead to negative (depressed) CMB topography, while upwellings cause positive (elevated) topography. Similar to our results, they also find that thermochemical models lead to an overall reduction in magnitude of CMB topography with respect to isochemical models.

[58] The two blobs of high density in the lowermost mantle, underlying large-scale low-density regions beneath the Pacific and Africa, are the most prominent features of our resulting density model. These low-density regions are, to a large part, actively upwelling, in agreement with results by *Gurnis et al.* [2000] and *Simmons et al.* [2007]. The high-density blobs beneath them are also present in the density model of *Ishii and Tromp* [2004], derived from seismology. They can be interpreted as chemically distinct material, which has been, due to flow in the overlying mantle, moved toward and accumulated beneath two large-scale upwellings beneath the Pacific and Africa.

[59] Our results therefore add further support to the existing evidence for compositional differences in the lowermost mantle from seismology, geochemistry and geodynamics: Some of the evidence from seismology has been cited above; many of the geochemical arguments for chemical variations are summarized by *Kellogg et al.* [1999]. *Davaille* [1999] conducted experiments to show that thermochemical domes, which may be dynamically stable over long time periods, and responsible for the observed "superswells", may coexist with narrow plumes responsible for "hot spots". *Torsvik et al.* [2006] and *Burke et al.* [2008] show that plumes appear to have risen mainly from the edges of Large Low Shear Velocity Provinces in the lowermost mantle, and take this as evidence that these are chemically distinct and stable over 200–300 Ma. *McNamara and Zhong* [2005] show that Earth's subduction history can lead to thermochemical structures similar in shape to the observed large, lower-mantle velocity anomalies. A chemically distinct lowermost mantle promises to offer a solution to the long-standing controversy over whole versus layered mantle convection.

[60] The motivation for this study was the fact that CMB topography is an important boundary condition for core dynamics, but it is poorly determined through seismology. There are only small areas on the CMB with a sufficient density of *PKKP* underside reflection points to make them useful in determining its topography [*Garcia and Souriau*, 2000]. Here we have therefore derived a model of CMB topography from mantle dynamics. Our CMB topography

model should be useful at least at long wavelengths of several thousand kilometers. At shorter wavelengths, density models in the lowermost mantle, and hence CMB topography models derived from them become unreliable.

[61] Based on our results, we expect that the thermal boundary layer at the base of the mantle is on average around 300 km thick, about the same as the region with the strongest chemical variations. We expect the temperature drop in this layer to be about 1000–1200 K, from about 3500–3700 K at the CMB to about 2500 K at the base of the mantle adiabat. However, the same viscosity drop across D'' could also correspond to a larger temperature difference, if dislocation creep is dominant is D'', a possibility, e.g., suggested by *Yamazaki and Karato* [2001].

[62] CMB heat flux and its lateral variation is another important boundary condition for core dynamics: Our preferred heat flux profiles imply a basal heat flux of about 15–20 TW, which may include heat from the core and from chemically distinct material at the base of the mantle. On the other hand, basal heat flux Q_c can also be estimated from boundary layer thickness and temperature drop:

$$Q_c = 4 \cdot \pi \cdot (r_{cmb} + 0.5 \cdot d_{th})^2 \cdot \kappa \cdot C_p \cdot \rho \cdot (T_{cmb} - T_{cmb,ad})/d_{th}.$$

[63] With heat capacity $C_p = 1250$ J/kg/K and diffusivity $\kappa = 1.5 \cdot 10^{-6}$ m^2/s, roughly consistent with a number of considerations as summarized by *Schubert et al.* [2001], and our preferred values $d_{th} = 300$ km and $T_{cmb} - T_{cmb,ad}$ between 1000 and 1200 K we obtain only between 5.7 and 6.8 TW. However, there are a number of ways to increase this number: Figures 6 and 8 show that almost as good results can be obtained with $T_{cmb} = 4000$ K and $d_{th} = 175$ km, corresponding to a temperature gradient which matches a seismological determination beneath the western Pacific [*Kuo and Chen*, 2005]. With these numbers, $Q_c = 14.1$ TW. Heat flux can also be higher if there are strong variations in thermal boundary layer thickness, e.g., due to the presence of subducted slabs. *Yoshida and Ogawa* [2005] as well as *Mittelstaedt and Tackley* [2006] point out that a large part of core heat flux may be due to warming of slabs settling on the CMB. *van der Hilst et al.* [2007] consider such lateral variations and obtain a global heat loss across the CMB between 7.5 and 15 TW, with the higher value approximately corresponding to the thermal diffusivity value adopted here. Heat flux may be further increased if there is additional heat transport through small-scale convection in the thermal boundary, due to reduced viscosity. Like the density model on which they are based, our flow models are up to spherical harmonic degree 31 and therefore do not include such small-scale convection. Furthermore, a larger temperature difference and hence larger heat flow through the lower boundary layer would result if the temperature profile outside the boundary layers was sub-adiabatic instead of adiabatic as assumed here. The radial mantle density profile determined by seismology, e.g., in PREM cannot be distinguished from an adiabatic profile outside the boundary layers; however, numerical mantle convection models often predict a strongly subadiabatic temperature profile [e.g., *Bunge*, 2005].

[64] The model presented here is intentionally simple; large scale only, no lateral viscosity variations, instantaneous flow computation only. We expect that the results obtained, such as viscosity and temperature profiles and large-scale density models, can provide a basis for future, more sophisticated models at higher resolution (including small-scale convection), and with more realistic rheology and time dependence. This could then, for example, yield further insights into CMB topography and heat flow and its lateral variations, and into questions such as whether there are chemically distinct high-density blobs above the CMB, and if so, whether they are stable for long times, are pulsating, or become entrained in mantle flow.

References

Asari, S., H. Shimizu, and H. Utada (2006), Variability of the topographic core-mantle torque calculated from core surface flow models, *Phys. Earth Planet. Inter.*, *154*, 85–111.

Becker, T. W. (2006), On the effect of temperature and strain-rate dependent viscosity on global mantle flow, net rotation, and plate-driving forces, *Geophys. J. Int.*, *167*, 943–957.

Becker, T. W., and L. Boschi (2002), A comparison of tomographic and geodynamic mantle models, *Geochem. Geophys. Geosyst.*, *3*(1), 1003, doi:10.1029/2001GC000168.

Becker, T. W., and R. J. O'Connell (2001), Predicting plate velocities with mantle circulation models, *Geochem. Geophys. Geosyst.*, *2*(12), doi:10.1029/2001GC000171.

Becker, T. W., V. Schulte-Pelkum, D. K. Blackman, J. B. Kellogg, and R. J. O'Connell (2006), Mantle flow under the western United States from shear wave splitting, *Earth Planet. Sci. Lett.*, *247*, 235–251.

Behn, M. D., C. P. Conrad, and P. G. Silver (2004), Detection of upper mantle flow associated with the African Superplume, *Earth Planet. Sci. Lett.*, *224*, 259–274.

Boehler, R. (1996), Melting temperature of the Earth's mantle and core: Earth's thermal structure, *Annu. Rev. Earth Planet. Sci.*, *24*, 15–40.

Brodholt, J. P., G. Helffrich, and J. Trampert (2007), Chemical versus thermal heterogeneity in the lower mantle: The most likely role of ane-lasticity, *Earth Planet. Sci. Lett.*, *262*, 429–437.

Bunge, H.-P. (2005), Low plume excess temperature and high core heat flux inferred from non-adiabatic geotherms in internally heated mantle circulation models, *Phys. Earth Planet. Inter.*, *153*, 3–10.

Burke, K., B. Steinberger, T. H. Torsvik, and M. A. Smethurst (2008), Plume generation zones at the margins of large low shear velocity provinces on the the core-mantle boundary, *Earth Planet. Sci. Lett.*, doi:10.1016/j.epsl.2007.09.042.

Calderwood, A. R. (1999), Mineral physics constraints on the temperature and composition of the Earth's mantle, Ph.D. thesis, University of British Columbia, Vancouver, B.C.

Cammarano, F., S. Goes, P. Vacher, and D. Giardini (2003), Inferring upper mantle temperatures from seismic velocities, *Phys. Earth Planet. Inter.*, *138*, 197–222.

Chudinovskikh, L., and R. Boehler (2007), Eutectic melting in the system FeS to 44 GPa, *Earth Planet. Sci. Lett.*, *257*, 97–103.

Davaille, A. (1999), Simultaneous generation of hotspots and superswells by convection in a heterogeneous planetary mantle, *Nature*, *402*, 756–760.

DeMets, C., R. G. Gordon, D. F. Argus, and S. Stein (1990), Current plate motions, *Geophys. J. Int.*, *101*, 425–478.

Doornbos, D. J., and T. Hilton (1989), Models of core-mantle boundary and the travel times of internally reflected core phases, *J. Geophys. Res.*, *94*(B11), 15,741–15,751.

Duffy, T. S., and D. L. Anderson (1989), Seismic velocities in mantle minerals and the mineralogy of the upper mantle, *J. Geophys. Res.*, *94*(B2), 1895–1912.

Dziewonski, A. M., and D. L. Anderson (1981), Preliminary reference Earth model, *Phys. Earth Planet. Inter.*, *25*, 297–356.

Forte, A. M., and J. X. Mitrovica (2001), Deep-mantle high-viscosity flow and thermomechanical structure inferred from seismic and geodynamic data, *Nature*, *410*, 1049–1056.

Forte, A. M., J. X. Mitrovica, and R. L. Woodward (1995), Seismic-geodynamic determination of the origin of excess ellipticity of the core-mantle boundary, *Geophys. Res. Lett.*, *22*(9), 1013–1016.

Garcia, R., and A. Souriau (1998), Mapping the core-mantle boundary topography from PKKP travel times, *The 6th Symposium of Study of the Earth's Deep Interior*, July 5–10, Tours, France (abstract).

Garcia, R., and A. Souriau (2000), Amplitude of the core-mantle boundary topography estimated by stochastic analysis of core phases, *Phys. Earth Planet. Inter.*, *117*, 345–359.

Gurnis, M., J. X. Mitrovica, J. Ritsema, and H.-J. van Heijst (2000), Constraining mantle density structure using geological evidence of surface uplift rates: The case of the African superplume, *Geochem. Geophys. Geosyst.*, *1*(7), doi:10.1029/1999GC000035.

Gwinn, C. R., T. A. Herring, and I. I. Shapiro (1986), Geodesy by radio interferometry: Studies of the forced nutations of the Earth. 2. Interpretation, *J. Geophys. Res.*, *91*(B5), 4755–4765.

Hager, B. H., and R. J. O'Connell (1979), Kinematic models of large-scale mantle flow, *J. Geophys. Res.*, *84*(B3), 1031–1048.

Hager, B. H., and R. J. O'Connell (1981), A simple global model of plate dynamics and mantle convection, *J. Geophys. Res.*, *86*(B6), 4843–4867.

Hernlund, J. W., and S. Labrosse (2007), Geophysically consistent values of the perovskite to post-perovskite transition Clapeyron slope, *Geophys. Res. Lett.*, *34*, L05309, doi:10.1029/2006GL028961.

Hide, R. (1969), Interaction between the earth's liquid core and solid mantle, *Nature*, *222*, 1055–1056.

Hirose, K., R. Sinmyo, N. Sata, and Y. Ohishi (2006), Determination of post-perovskite phase transition boundary in MgSiO3 using Au and MgO pressure standards, *Geophys. Res. Lett.*, *33*, L01310, doi:10.1029/2005GL024468.

Hofmeister, A. M. (2005), Earth's heat flux revised and linked to chemistry, *Tectonophysics*, *395*, 159–177.

Ishii, M., and J. Tromp (2004), Constraining large-scale mantle heterogeneity using mantle and inner-core sensitive normal modes, *Phys. Earth Plan. Inter.*, *146*, 113–124.

Ita, J. J., and L. Stixrude (1992), Petrology, elasticity, and composition of the mantle transition zone, *J. Geophys. Res.*, *97*(B5), 6849–6866.

Kellogg, L. H., B. H. Hager, and R. D. van der Hilst (1999), Compositional stratification in the deep mantle, *Science*, *283*, 1881–1884.

Korenaga, J. (2007), Eustasy, supercontinental insulation, and the temporal variability of terrestrial heat flux, *Earth Planet. Sci. Lett.*, *257*, 350–358.

Kuang, W. J., and B. F. Chao (2001), Topographic core-mantle coupling in geodynamo modeling, *Geophys. Res. Lett.*, *28*(9), 1871–1874.

Kuo, B.-Y., and C.-W. Chen (2005), A seismological determination of the temperature gradient in D″ beneath the western Pacific, *J. Geophys. Res.*, *110*, B05304, doi:10.1029/2004JB003291.

Lassak, T. M., A. K. McNamara, and S. Zhong (2007), Influence of thermochemical piles on topography at Earth's CMB, *Earth Planet. Sci. Lett.*, *261*, 443–455.

Masters, G., G. Laske, H. Bolton, and A. Dziewonski (2000), The relative behavior of shear velocity, bulk sound speed, and compressional velocity in the mantle: Implications for chemical and thermal structure, in *Seismology and Mineral Physics*, *Geophys. Monogr. Ser.*, vol. 117, edited by S. Karato, pp. 63–87, AGU, Washington, D. C.

Mathews, P. M., T. A. Herring, and B. A. Buffett (2002), Modeling of nutation and precession: New nutation series for nonrigid Earth and insights into the Earth's interior, *J. Geophys. Res.*, *107*(B4), 2068, doi:10.1029/2001JB000390.

McNamara, A. K., and S. Zhong (2005), Thermochemical structures beneath Africa and the Pacific Ocean, *Nature*, *437*, 1136–1139.

Mitrovica, J. X. (1996), Haskell [1935] revisited, *J. Geophys. Res.*, *101*(B1), 555–569.

Mitrovica, J. X., and A. M. Forte (2004), A new inference of mantle viscosity based upon joint inversion of convection and glacial isostatic adjustment data, *Earth. Planet. Sci. Lett.*, *225*, 177–189.

Mittelstaedt, E., and P. J. Tackley (2006), Plume heat flow is much lower than CMB heat flow, *Earth Planet. Sci. Lett.*, *241*, 202–210.

Moucha, R., A. M. Forte, J. X. Mitrovica, and A. Daradich (2007), Lateral variations in mantle rheology: Implications for convection related surface observables and inferred viscosity models, *Geophys. J. Int.*, *169*, 113–135, doi:10.1111/j.1365-246X.2006.03225.x.

Murakami, M., K. Hirose, K. Kawamura, N. Sata, and Y. Ohishi (2004), Post-perovskite phase transition in MgSiO3, *Science*, *304*, 855–858.

Oganov, A. R., and S. Ono (2004), Theoretical and experimental evidence for a post-perovskite phase of MgSiO3 in Earth's D″ layer, *Nature*, *430*, 445–448.

Pollack, H. N., S. J. Hurter, and J. R. Johnson (1993), Heat loss from the Earth's interior: Analysis of the global data set, *Rev. Geophys.*, *31*(3), 267–280.

Ricard, Y., L. Fleitout, and C. Froidevaux (1984), Geoid heights and lithospheric stresses for a dynamic Earth, *Ann. Geophys.*, *2*, 267–286.

Richards, M. A., and B. H. Hager (1984), Geoid anomalies in a dynamic Earth, *J. Geophys. Res.*, *89*, 5987–6002.

Ritsema, J., and H. J. van Heijst (2000), Seismic imaging of structural heterogeneity in Earth's mantle: Evidence for large-scale mantle flow, *Sci. Progr.*, *83*, 243–259.

Rodgers, A., and J. Wahr (1993), Inference of core-mantle boundary topography from ISC *PcP* and *PKP* traveltimes, *Geophys. J. Int.*, *115*, 991–1011.

Schubert, G., D. L. Turcotte, and P. Olson (2001), *Mantle Convection in the Earth and Planets*, Cambridge Univ. Press, Cambridge, UK.

Sidorin, I., M. Gurnis, and D. V. Helmberger (1999), Evidence for a ubiquitous seismic discontinuity at the base of the mantle, *Science*, *286*, 1326–1331.

Simmons, N. A., A. M. Forte, and S. P. Grand (2006), Constraining mantle flow with seismic and geodynamic data: A joint approach, *Earth Planet. Sci. Lett.*, *246*, 109–124.

Simmons, N. A., A. M. Forte, and S. P. Grand (2007), Thermochemical structure and dynamics of the African superplume, *Geophys. Res. Lett.*, *34*, L02301, doi:10.1029/2006GL028009.

Soldati, G., and L. Boschi (2005), The resolution of whole Earth seismic tomographic models, *Geophys. J. Int.*, *161*, 143–153.

Steinberger, B., and A. R. Calderwood (2006), Models of large-scale viscous flow in the Earth's mantle with constraints from mineral physics and surface observations, *Geophys. J. Int.*, *167*, 1461–1481.

Steinberger, B., H. Schmeling, and G. Marquart (2001), Large-scale lithospheric stress field induced by global mantle circulation, *Earth Planet. Sci. Lett.*, *186*, 75–91.

Steiner, S. A., and C. P. Conrad (2007), Does active mantle upwelling help drive plate motions?, *Phys. Earth Planet. Inter.*, *161*, 103–114.

Su, W.-J., and A. M. Dziewonski (1997), Simultaneous inversion for 3-D variations in shear and bulk velocity in the mantle, *Phys. Earth Planet. Inter.*, *100*, 135–156.

Sze, E., and R. D. van der Hilst (2003), Core mantle boundary topography from short period PcP, PKP, and PKKP data, *Phys. Earth Planet. Inter.*, *135*, 27–46.

Thoraval, C., and M. A. Richards (1997), The geoid constraint in global geodynamics: Viscosity structure, mantle heterogeneity models and boundary conditions, *Geophys. J. Int.*, *131*, 1–8.

Torsvik, T. H., M. A. Smethurst, K. Burke, and B. Steinberger (2006), Large igneous provinces generated from the margins of the large low-velocity provinces in the deep mantle, *Geophys. J. Int.*, *167*, 1447–1460.

Trampert, J., F. Deschamps, J. Resovsky, and D. Yuen (2004), Probabilistic tomography maps chemical heterogeneities throughout the lower mantle, *Science*, *306*, 853–856.

Tsuchiya, T., J. Tsuchiya, K. Umemoto, and R. M. Wentzcovitch (2004), Phase transition in MgSiO$_3$ perovskite in the earth's lower mantle, *Earth Planet. Sci. Lett.*, *224*, 241–248.

van der Hilst, R. D., M. V. de Hoop, P. Wang, S.-H. Shim, P. Ma, and L. Tenorio (2007), Seismostratigraphy and thermal structure of Earth's core-mantle boundary region, *Science*, *315*, 1813–1817.

Wang, Z. W. (1999), The melting of Al-bearing perovskite at the core-mantle boundary, *Phys. Earth Planet. Inter.*, *115*, 219–228.

Wang, Y., and L. Wen (2004), Mapping the geometry and geographic distribution of a very low velocity province at the base of the Earth's mantle, *J. Geophys. Res.*, *109*, B10305, doi:10.1029/2003JB002674.

Wei, M., and D. Sandwell (2006), Estimates of heat flow from Cenozoic seafloor using global depth and age data, *Tectonophysics*, *417*, 325–335.

Wessel, P., and W. H. F. Smith (1998), New, improved version of the generic mapping tools released, *Eos Trans. AGU*, *79*, 579.

Yamazaki, D., and S.-I. Karato (2001), Some mineral physics constraints on the rheology and geothermal structure of Earth's lower mantle, *Am. Mineral.*, *86*, 385–391.

Yoshida, M., and M. Ogawa (2005), Plume heat flow in a numerical model of mantle convection with moving plates, *Earth Planet. Sci. Lett.*, *239*, 276–285.

Zerr, A., and R. Boehler (1994), Constraints on the melting temperature of the lower mantle from high-pressure experiments on MgO and magnesiowüstite, *Nature*, *371*, 506–508.

———————————

R. Holme, Department of Earth and Ocean Sciences, University of Liverpool, 4 Brownlow Street, Liverpool L69 3GP, UK. (holme@liv.ac.uk)

B. Steinberger, Center for Geodynamics, Geological Survey of Norway, Leiv Eirikssons vei 39, N-7491 Trondheim, Norway. (bernhard.steinberger@ngu.no)